Charged-current exclusive pion production in neutrino-deuterium interactions

T. Kitagaki, H. Yuta, S. Tanaka, A. Yamaguchi, K. Abe, K. Hasegawa,
K. Tamai, S. Kunori,* Y. Otani,† H. Hayano,‡ H. Sagawa,‡ K. Akatsuka,§ and K. Furuno
Tohoku University, Sendai, Japan

N. J. Baker, A. M. Cnops,** P. L. Connolly,†† S. A. Kahn, H. G. Kirk, M. J. Murtagh,
R. B. Palmer, N. P. Samios, and M. Tanaka
Brookhaven National Laboratory, Upton, New York 11973

M. Higuchi and M. Sato
Tohoku Gakuin University, Sendai, Japan
(Received 17 March 1986)

High-statistics data from two exposures of the BNL 7-foot deuterium bubble chamber to a wide-band-neutrino beam with an average energy of 1.6 GeV were analyzed for exclusive pion production in charged-current neutrino-deuterium interactions. For the single-pion production reactions, the properties of Δ^{++} production and decay as well as the final results of an isospin analysis are presented. New results for single-pion and multipion production are also presented.

I. INTRODUCTION

Exclusive pion production in ν_μ-nucleon charged-current reactions has been studied in several bubble-chamber experiments.[1-7] These experiments have primarily investigated the properties of $\Delta(1232)$ production and decay as well as the isospin structure of the π-nucleon system in single-pion production. However, the properties of exclusive multipion production have been studied only in two other experiments.[2,3]

In this paper, exclusive pion production processes in charged-current neutrino interactions are investigated using data from a high-statistics experiment carried out at Brookhaven National Laboratory using the 7-foot bubble chamber filled with deuterium and the Alternating Gradient Synchrotron (AGS) wide-band neutrino beam. The analysis of Δ^{++} production and decay are presented and compared to theoretical predictions. The isospin properties of the π-nucleon system for single-pion production and new results on multipion production are also presented.

The experiment was carried out in two runs. A total of 1 800 000 photographs were taken during the two runs. The experimental conditions were similar in each run. The 7-foot bubble chamber was located approximately 100 m from the neutrino production target. Mesons produced in this target by the 29-GeV/c proton beam from the AGS were focused by a double-horn system and then traversed a 57-m decay space in which a few percent of the π's and K's decayed into neutrinos. The decay space was followed by 30 m of iron to absorb the remaining hadrons. The resultant neutrino flux in the chamber peaked at 1.2 GeV and extended up to $\sim$15 GeV. The 7-foot bubble chamber was equipped with three 70-mm cameras and operated in a 25-kG magnetic field. For identification of muon tracks, four 1.5-m$\times$1.8-m$\times$5-cm-thick stainless-steel plates were installed in the downstream region of the chamber for the first run. To improve the identification of low-energy muon tracks, this plate was replaced by three 1.5-m$\times$1.8-m$\times$1.75-cm-thick plates for the second run. The results from the first exposure have been published.[7-9] The combined data of the two exposures are used in this study.

II. EVENT SELECTION

A. Scanning and measuring procedures

The film was scanned for neutral-induced events with more than one track visible in the chamber. Approximately 32% of the film was rescanned and the scanning efficiency as a function of event topology is listed in Table I. The average scanning efficiency was 93%. All events were measured and processed through both the geometry program TVGP and the kinematic-fitting program SQUAW. Events that failed in the first measurement were remeasured. All events were reviewed by physicists to check the results of the measurements and to make visual particle identification using ionization information. The overall measuring efficiencies for events in the fiducial volume are also listed in Table I.

B. Selection of the charged-current event sample

The events obtained from the measurement contain not only neutrino-induced events but also background-induced events by neutral and charged hadrons. Events with acceptable four-constraint (4C) fits to the $pp\rightarrow pp$ or $\pi^\pm p\rightarrow\pi^\pm p$ hypotheses were removed from the sample. After this cut, 14 719 events remained. Neutrino charged-current events were selected by imposing the following requirements: (1) the magnitude of the total-visible-momentum vector $\mathbf{P}_{\rm vis}$ must be greater than 150 MeV/c, (2) the angle between the total-visible-momentum

TABLE I. Scanning and measuring efficiency.

Number of prongs	Scanning efficiency: Single scan	Scanning efficiency: Average (including double scan)	Measuring efficiency
All	0.90±0.01	0.93±0.01	0.97±0.02
2	0.86±0.01	0.90±0.01	0.99±0.02
3	0.93±0.01	0.95±0.01	0.96±0.02
4	0.93±0.02	0.95±0.02	0.93±0.07
5	0.93±0.02	0.95±0.02	0.94±0.08
6–9	0.93±0.02	0.95±0.02	0.94±0.18

vector and the neutrino-beam direction must be less than 50°, and (3) at least one of the negative tracks must either leave the chamber without interacting or stop in the plate with a range consistent with a muon interpretation or decay into an electron. After these cuts, 12 963 events remained. About 91% of the events were two- and three-prong events.

To improve the measurement quality, events in a fiducial volume of 4 m^3 were selected. This fiducial volume ensured a minimum track length of 20 cm from the vertex to either the first iron plate installed in the chamber or to the downstream chamber wall. A total of 9203 events were in the fiducial volume. Events which did not have a net charge of 0 or +1 were also removed from the sample. This reduced the number of events to 8960 and this data set will be used throughout the following analysis.

TABLE II. Corrections for the single-pion production reactions.

Correction		Correction factor
(a) $\nu d \to \mu^- p \pi^+ n_s$		
Background	g_1	0.98±0.01
Scanning-measuring efficiency	g_2	1.07±0.05
χ^2 probability cut	g_3	1.01
H_2 contamination in D_2	g_4	0.87±0.02
Loss of fast neutron spectators	g_5	1.22±0.01
Total correction $g_1 \times g_2 \times g_3 \times g_4 \times g_5$		1.12±0.07
(b) $\nu d \to \mu^- p \pi^0 p_s$		
Background from		
$\mu^- p \pi^0 \pi^0$ and $\mu^- n \pi^+ \pi^0$	f_1	−0.202±0.018
$\mu^- p$ and $\mu^- n \pi^+$	f_2	−0.032±0.012
$\nu p \pi^-$	f_3	−0.084±0.014
$nn \to np\pi^-$	f_4	−0.154±0.043
Event assigned to $\mu^- n \pi^+$ and $\mu^- p$	f_5	+0.235±0.071
Scanning-measuring efficiency	g_1	1.13 ±0.06
Correction for three prong	g_2	1.22 ±0.01
Total correction $(1+f_1+f_2+f_3+f_4)g_1g_2$		1.05 ±0.14
(c) $\nu d \to \mu^- n \pi^+ p_s$		
Background from		
$\mu^- p \pi^0 \pi^0$ and $\mu^- n \pi^+ \pi^0$	f_1	−0.277±0.021
$\mu^- p$ and $\mu^- p \pi^0$	f_2	−0.129±0.063
$\nu p \pi^-$	f_3	−0.021±0.004
$nn \to np\pi^-$	f_4	−0.031±0.016
Event assigned to $\mu^- p \pi^0$ and $\mu^- p$	f_5	+0.024±0.016
Correction for θ_{vis} and P_{vis} cuts	f_6	+0.083±0.049
Scanning-measuring efficiency	g_1	1.13 ±0.06
Correction for three prong	g_2	1.22 ±0.01
Total correction $(1+f_1+\cdots+f_6)g_1g_2$		0.890±0.103

C. The $\mu^- p$ and $\mu^- p\pi^+$ events

The $\mu^- p$ and $\mu^- p\pi^+$ events were selected from the charged-current event sample using three-constraint (3C) kinematical fits, since the neutrino-beam direction is known to an accuracy of 0.5°. The 3C fits were performed on the two- and three-prong events using the two hypotheses

$$\nu_\mu d \to \mu^- p p_s \ , \tag{1}$$

$$\nu_\mu d \to \mu^- p \pi^+ n_s \ , \tag{2}$$

where p_s and n_s are the spectator proton and neutron, respectively. If the spectator nucleon was not measured, an initial value of 0 ± 45 MeV/c for P_x, P_y, and P_z of the spectator was assigned in the fit.

The χ^2 probability distribution, $P(\chi^2)$, for the 3C-fit events was uniformly distributed for reaction (1) in the range of $P(\chi^2)>1\%$. The distribution for reaction (2) peaked toward $P(\chi^2)=100\%$. This peak in reaction (2) is attributed to some hydrogen contamination in the deuterium. The events with $P(\chi^2)<1\%$ were dominated by other reactions. Requiring that the χ^2 probability be greater than 1% and that the particle identification be consistent with the fit hypotheses, we obtained 2684 $\nu_\mu d \to \mu^- p p_s$ events and 1610 $\nu_\mu d \to \mu^- p \pi^+ n_s$ events, where we took the hypothesis with the highest χ^2 probability for events with multiple fits.

The contamination from the reaction $\nu_\mu d \to \mu^- p \pi^+ \pi^0 n_s$ to the $\nu_\mu d \to \mu^- p \pi^+ n_s$ sample was estimated by examining the 3C $\nu_\mu d \to \mu^- p \pi^+ \pi^- p_s$ events. The background was estimated to be 2%. The background from other sources such as $\nu p \to \nu p \pi^+ \pi^-$ was estimated to be less than 1%. In addition, corrections were made for a $(13\pm2)\%$ hydrogen contamination[7] in the deuterium and a loss of $(22\pm1)\%$ of the events due to the fast spectator neutron. After all corrections including the scanning and measuring efficiencies we obtained 1803 $\mu^- p\pi^+$ events. The corrections for the $\mu^- p\pi^+$ events are listed in Table II(a).

D. The reactions $\mu^- p\pi^0$ and $\mu^- n\pi^+$

Since there are no kinematic constraints for the reactions

$$\nu_\mu d \to \mu^- p \pi^0 p_s \tag{3}$$

and

$$\nu_\mu d \to \mu^- n \pi^+ p_s \ , \tag{4}$$

we use the results of the zero-constraint (0C) calculation and particle identification to study reactions (3) and (4). To avoid a potential ambiguity between the recoil proton and the spectator proton in the three-prong event sample, we used only the two-prong events and corrected for the unused three-prong events. About 15% of the events were ambiguous between reactions (3) and (4). These events were assigned to both final states with a weight of one half. The final data sample contains 853.5 $\mu^- p\pi^0$ events and 822.5 $\mu^- n\pi^+$ events.

The following backgrounds and losses have been studied using the events obtained from this experiment: (1) neutrino-induced multipion background, (2) neutral-current background, (3) neutron-induced background, (4) contamination from the $\mu^- p$ channel, (5) event loss due to miss fit to the reaction $\nu n \to \mu^- p$, (6) losses coming from $\theta_{\rm vis}$ and $P_{\rm vis}$ cuts, (7) misassignment of the $\mu^- p\pi^0$ events to the $\mu^- n\pi^+$ sample and vice versa, and (8) correction for the unused three-prong events. The methods used to estimate these effects were similar to those described in Ref. 7.

After these corrections, we obtained 896 $\mu^- p\pi^0$ events and 732 $\mu^- n\pi^+$ events. The estimated backgrounds and losses are summarized in Tables II(b) and II(c), and the raw and corrected event numbers for these reactions are given in Table III.

TABLE III. Observed and corrected event numbers.

Reaction	Observed	Corrected
$\mu^- p\pi^+$	1610	1803
$\mu^- p\pi^0$	853.5	896
$\mu^- n\pi^+$	822.5	732

E. Multipion states

The multipion reactions

$$\nu_\mu d \to \mu^- p p_s \pi^+ \pi^- \ , \tag{5}$$

TABLE IV. Corrections for multipion reactions.

Reaction $\nu d \to$	$\mu^- p p_s$ $\pi^+\pi^-$	$\mu^- p n_s$ $\pi^+\pi^+\pi^-$	$\mu^- p p_s$ $\pi^+\pi^+\pi^-\pi^-$	$\mu^- p n_s$ $\pi^+\pi^+\pi^+\pi^-\pi^-$
Raw events	276	53	14	6
Correction		Correction factor		
Background	0.98	0.98	0.98	0.98
Scanning and measuring efficiency	1.16	1.16	1.16	1.16
Prob(χ^2)<1% cut	1.01	1.01	1.01	1.01
Loss due to fast spectator neutron		1.22		1.22
H_2 contamination		0.87		0.87
Corrected events	317	65	16	7.3

$$\nu_\mu d \to \mu^- p n_s \pi^+ \pi^+ \pi^- , \quad (6)$$

$$\nu_\mu d \to \mu^- p p_s \pi^+ \pi^+ \pi^- \pi^- , \quad (7)$$

$$\nu_\mu d \to \mu^- p n_s \pi^+ \pi^+ \pi^+ \pi^- \pi^- , \quad (8)$$

were selected from the charged-current event sample using 3C fits to the various mass hypotheses together with particle identification. The exclusive multipion channels with one or more neutral pions were not isolated because of the difficulty of estimating the backgrounds. Requiring that the 3C χ^2 probability be greater than 1% and that the particle identification be consistent with the mass hypothesis, we obtained 276 events of reaction (5), 53 events of reaction (6), 14 events of reaction (7), and 6 events of reaction (8). Of these events, 101, 21, 9, and 3 had μ^-/π^- or π^+/p ambiguities. For these ambiguous events, the fits with the highest χ^2 probability were accepted.

The contaminations in the 3C-fit reactions from final states with a π^0 were determined from the events with an additional charged pion by deleting the extra pion and then fitting the events. From this study, the contaminations were estimated to be 2% for each of reactions (5), (6), and (7). The same value was used for reaction (8) since no measurement was possible in this case. The numbers of raw and corrected events are listed in Table IV.

Figure 1 shows the fitted momentum distributions of the spectator protons for reactions (1), (5), and (7). The shaded areas represent the observed spectator protons which amount to ~21% of the total events in each channel except in reaction (7), where only one event had an observed spectator proton. The solid curves were calculated from the Hulthen wave function. They reproduce the data fairly well.

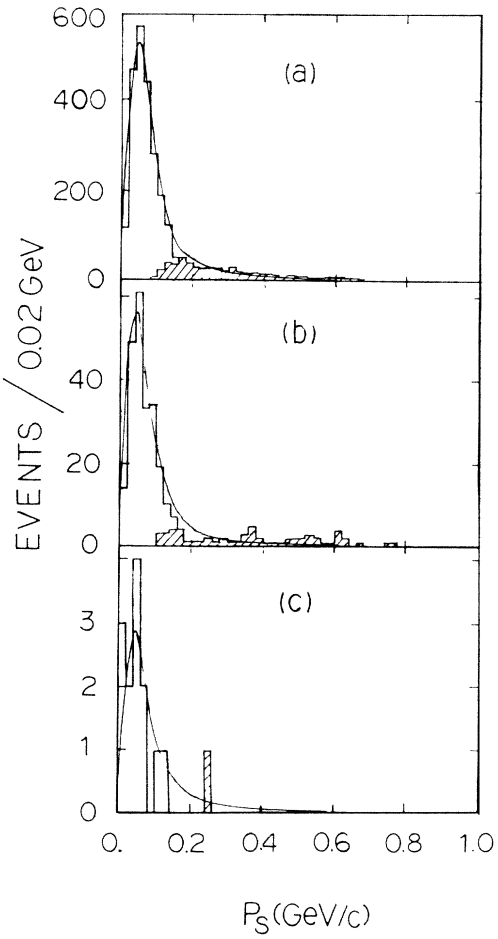

FIG. 1. Spectator-proton momentum distributions for (a) $\mu^- p p_s$, (b) $\mu^- p \pi^+ \pi^- p_s$, and (c) $\mu^- p \pi^+ \pi^+ \pi^- \pi^- p_s$ states. The shaded areas correspond to the observed spectator protons. The curves are the predictions of the Hulthen wave function normalized to the total number of events.

III. SINGLE-PION PRODUCTION

A. General features

Figures 2, 3, and 4 show the distributions in E_ν, Q^2, and the nucleon-pion invariant mass for the three single-pion channels, (2), (3), and (4). The distributions in E_ν and Q^2 are similar. In the $\mu^- p \pi^+$ channel, the $\Delta^{++}(1232)$ peak dominates the nucleon-pion mass distribution, but in the $\mu^- p \pi^0$ and $\mu^- n \pi^+$ final states, the $\Delta^+(1232)$ peaks are superimposed on a broader $N\pi$-mass distribution covering the region of 1.4—1.6 GeV.

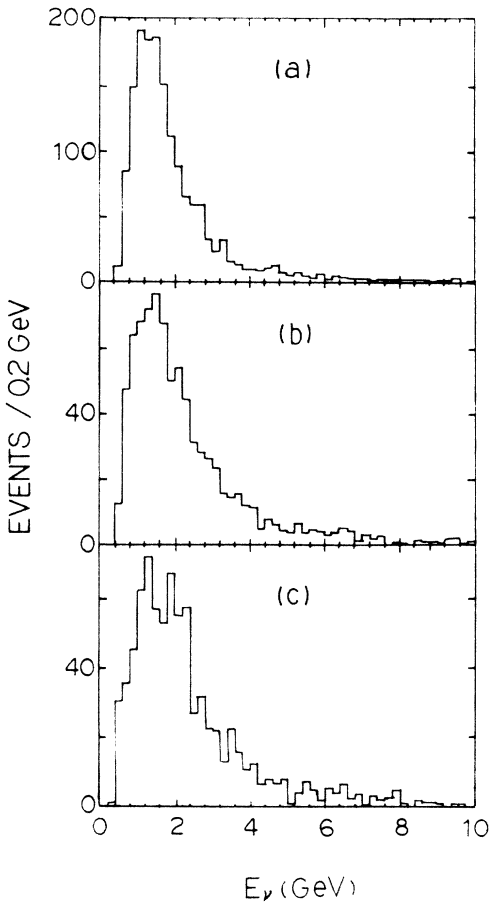

FIG. 2. The neutrino energy distributions (E_ν) for the final states (a) $\mu^- p \pi^+$, (b) $\mu^- p \pi^0$, and (c) $\mu^- n \pi^+$.

To search for exotic states the $\mu^-\pi$- and μ^-N-mass distributions for reactions (2), (3), and (4) are shown in Figs. 5 and 6. The shaded areas correspond to events with $N\pi$ masses >1.4 GeV. No significant peak is observed. The excess of events at 1.2 GeV in the μ^-p mass distribution in Fig. 6(b) comes in part from misassigned $\nu\pi^-p$ and $np\pi^-$ events, for which the background was estimated to be $\sim 24\%$ [Table II(b)].

The cross sections for the $\mu^-p\pi^+$, $\mu^-p\pi^0$, and $\mu^-n\pi^+$ states were measured using the corrected numbers of these events and the neutrino flux determined from the observed quasielastic events[8,10] in this experiment. A maximum-likelihood fit to the Q^2 distribution of quasielastic events in the range from 0.08 to 3 GeV^2 gave a value of the axial-vector mass $M_A=1.10\pm0.05$ GeV and this value was used in the determination of the neutrino flux.

Figure 7 shows the measured cross sections for the three final states $\mu^-p\pi^+$, $\mu^-p\pi^0$, and $n^-n\pi^+$. A rapid increase in the cross section is observed for the $\mu^-p\pi^+$ state in which Δ^{++} production is predominant. The cross section levels off above $E_\nu=1.5$ GeV. The cross sections for reactions (3) and (4) are increasing more gradually.

B. Δ^{++} production

Figure 8 shows the $p\pi^+$ effective mass distribution for the $\mu^-p\pi^+$ state in the neutrino energy range $E_\nu=0.5$–6.0 GeV. This energy range was chosen to avoid the uncertainty in the neutrino flux for $E_\nu>6.0$ GeV. There is a strong $\Delta^{++}(1232)$ signal and no other resonance is observed above the $\Delta^{++}(1232)$ mass region. The mass distribution was fitted over the mass range $M(p\pi^+)=1.08$–1.4 GeV using a relativistic Breit-Wigner resonance shape with a three-body phase-space background. The curve is the result of the best fit and it represents the data well. The values of the resonance mass M_R and the width Γ_R from the fit were

$$M_R=1.224\pm0.002 \text{ GeV},$$

$$\Gamma_R=0.101\pm0.006 \text{ GeV}.$$

The phase-space component obtained from the fit was less than 1%.

To study the spin properties of the $p\pi^+$ system, the π^+ angular distribution was analyzed in the $p\pi^+$ rest frame. The azimuthal angle ϕ and polar angle θ in this rest frame

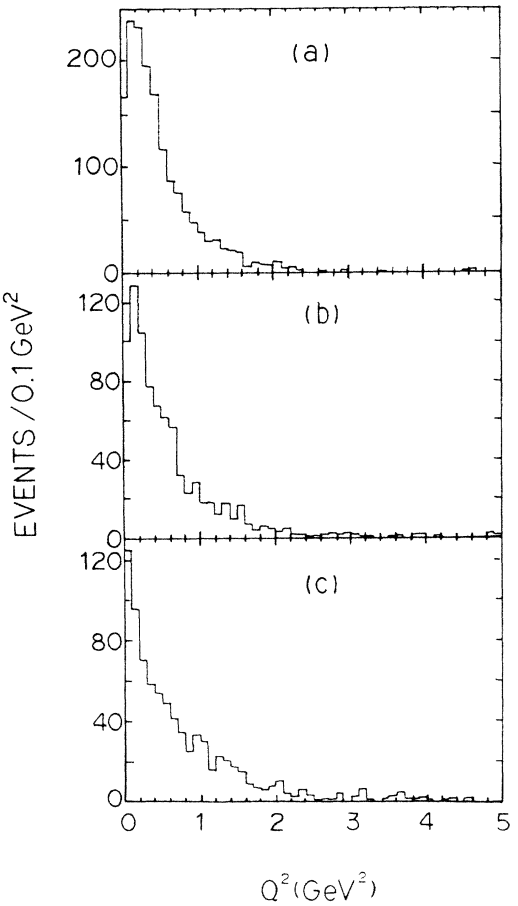

FIG. 3. The four-momentum-transfer-squared distributions (Q^2) for the final states (a) $\mu^-p\pi^+$, (b) $\mu^-p\pi^0$, and (c) $\mu^-n\pi^+$.

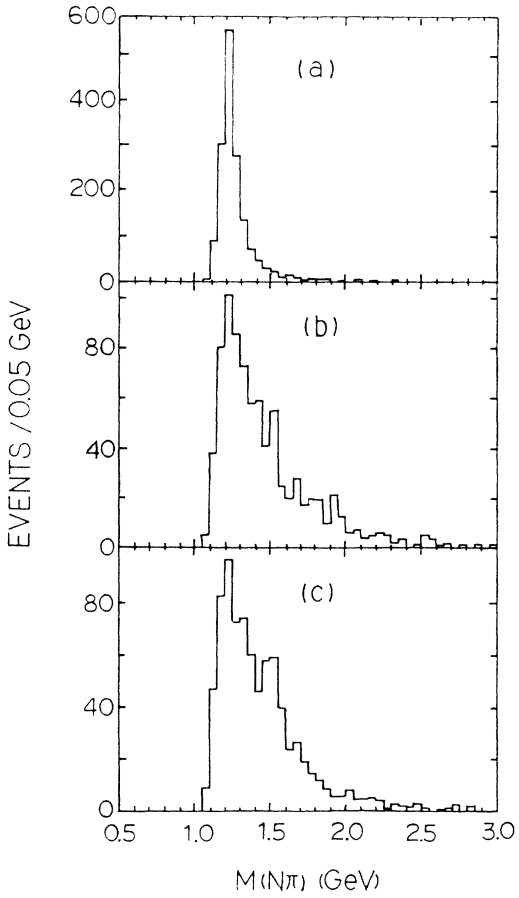

FIG. 4. The $N\pi$ invariant-mass $M(N\pi)$ distributions for the final states (a) $\mu^-p\pi^+$, (b) $\mu^-p\pi^0$, and (c) $\mu^-n\pi^+$.

are defined in a right-handed coordinate system, where the z axis is parallel to the momentum transfer $\mathbf{q}=\mathbf{p}_\nu-\mathbf{p}_\mu$ and the y axis is parallel to the normal to the production plane $\mathbf{p}_\nu\times\mathbf{p}_\mu$. Figure 9 shows the forward-backward asymmetry defined as

$$\alpha=\frac{N_F-N_B}{N_F+N_B},$$

where N_F and N_B are the numbers of the events with $\cos\theta>0$ and $\cos\theta<0$, respectively. The forward-backward asymmetry, α is nearly zero for $M(p\pi^+)<1.4$ GeV, but it increases rapidly for $M(p\pi^+)>1.4$ GeV. This suggests the presence of the pure spin state for $M(p\pi^+)<1.4$ GeV and of components other than a P-wave for $M(p\pi^+)>1.4$ GeV. For this reason, the $\mu^-p\pi^+$ events with $M(p\pi^+)<1.4$ GeV are selected as Δ^{++} events.

Figure 10 shows the Q^2 distribution for the events in the Δ^{++} mass region. The dip observed in the small-Q^2 region cannot be due to an experimental bias because the events are observed as three-prong events.

Schreiner and Von Hippel[11] made a comparison of the Q^2 distribution with the prediction of the Adler model[12] which is based on the $V-A$ theory with a nucleon-exchange mechanism. Following their formalism with a dipole axial-vector form factor, the axial-vector mass M_A

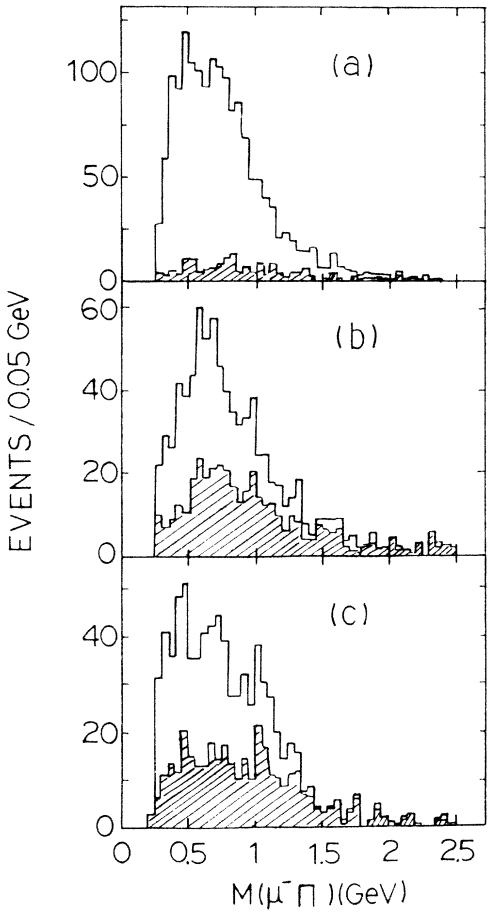

FIG. 5. The $\mu^-\pi$-mass distributions for (a) $\mu^-p\pi^+$, (b) $\mu^-p\pi^0$, and (c) $\mu^-n\pi^+$ final states. The slashed areas represent the events with $M(N\pi)>1.4$ GeV.

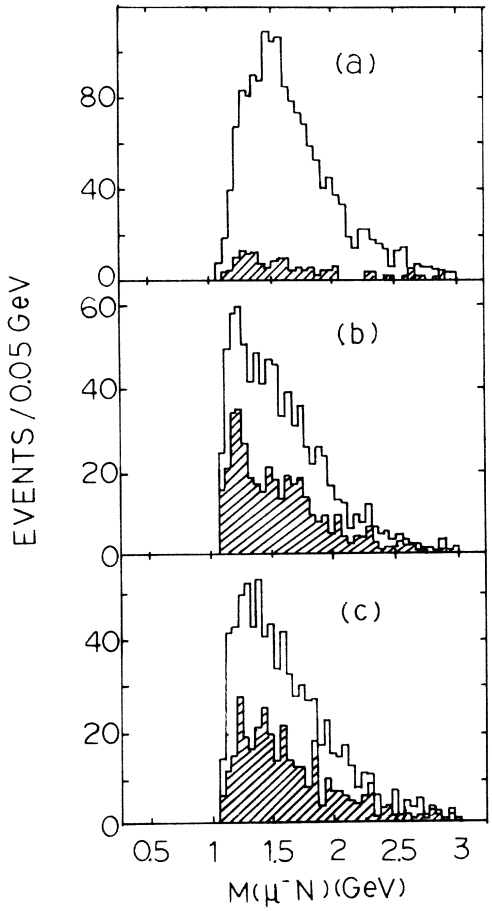

FIG. 6. The μ^-N-mass distributions for (a) $\mu^-p\pi^+$, (b) $\mu^-p\pi^0$, and (c) $\mu^-n\pi^+$ final states. The slashed areas represent the events with $M(N\pi)>1.4$ GeV.

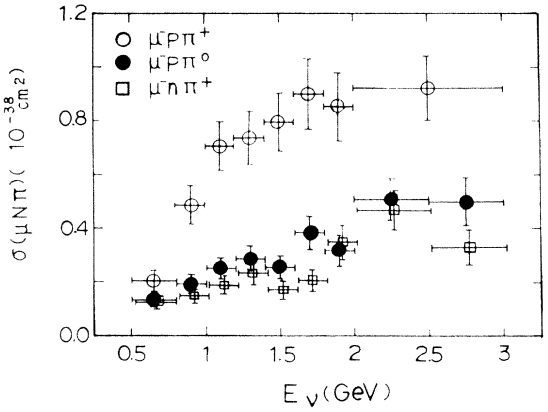

FIG. 7. The cross sections for the final states (a) $\mu^-p\pi^+$, (b) $\mu^-p\pi^0$, and (c) $\mu^-n\pi^+$.

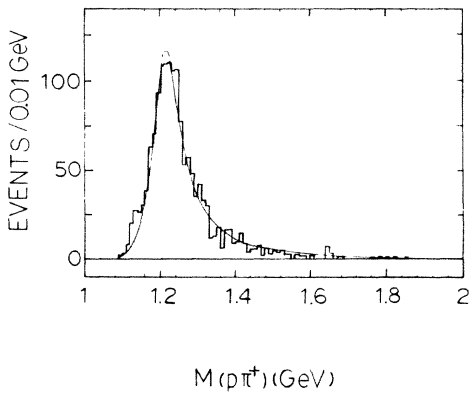

FIG. 8. The $p\pi^+$ invariant mass $M(p\pi^+)$ for $\mu^- p\pi^+$ events with $0.5 < E_\nu < 6.0$ GeV. The solid curve is the result of the best fit using a relativistic Breit-Wigner function and a three-body phase space.

obtained from the best fit using a maximum-likelihood method was

$$M_A = 1.28 \pm 0.11 \text{ GeV} \tag{9}$$

in the Q^2 region from 0.1 to 3.0 GeV^2. The prediction with $M_A = 1.28$ GeV (solid curve) describes the data satisfactorily, although there seems to be some deviation from the data in the low-Q^2 region.

Figure 11 shows the ratio of $(dN/dQ^2)_{\text{data}}$ to $(dN/dQ^2)_{\text{Adler}}$ for the $\mu^-\Delta^{++}$ events. The ratio decreases smoothly for $Q^2 < 0.4$ GeV^2 and deviates more than 3 from unity for $Q^2 < 0.05$ GeV^2. This deviation from unity for $Q^2 < 0.05$ GeV^2 could be due to nuclear effects which are expected in this low-Q^2 region.

Figures 12(a) and 12(b) show the Δ^{++} decay angular distributions of the π^+ in the polar and azimuthal angles θ and ϕ in the Δ^{++} rest frame, respectively. The decay angular distribution $dW(\theta,\phi)/d\Omega$ for the $\Delta^{++}(I=\frac{3}{2})$ decay is given by

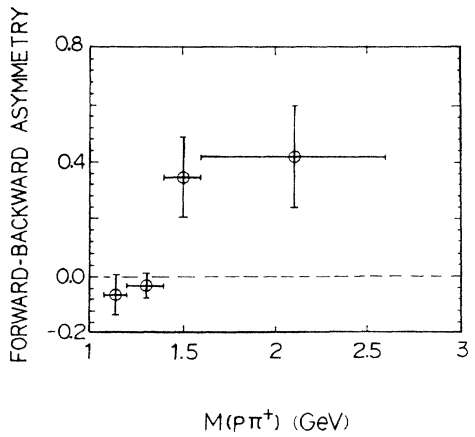

FIG. 9. $M(p\pi^+)$ dependence of the forward-backward asymmetry for the $\mu^- p\pi^+$ events with $0.5 < E_\nu < 6.0$ GeV.

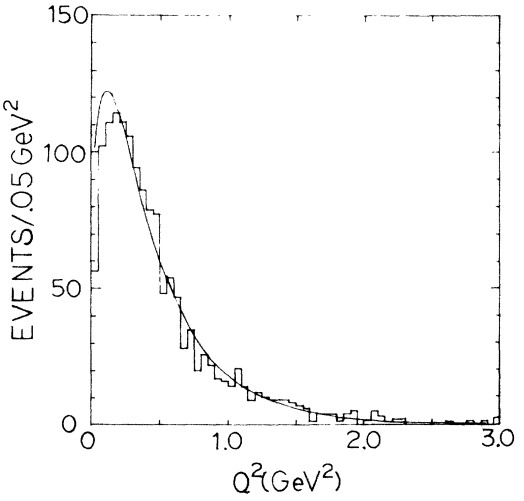

FIG. 10. Q^2 distribution for $\mu^- p\pi^+$ events with $M(p\pi^+) < 1.4$ GeV for $0.5 < E_\nu < 6.0$ GeV. The solid curve is the prediction of the Adler model with $M_A = 1.28$ GeV normalized to the events with $Q^2 > 0.02$ GeV^2.

$$dW(\theta,\phi)/d\Omega = \frac{1}{\sqrt{4\pi}} \left[Y_0^0 - \frac{2}{\sqrt{5}}(\tilde{\rho}_{33} - 0.5) Y_2^0 + \frac{4}{\sqrt{10}} \tilde{\rho}_{31} \mathrm{Re}(Y_2^1) - \frac{4}{\sqrt{10}} \tilde{\rho}_{3-1} \mathrm{Re}(Y_2^2) \right], \tag{10}$$

where Y_l^m is the spherical harmonic function and $\tilde{\rho}_{mn}$ is the reduced density matrix element and is given in terms of the density matrix elements ρ_{mn} by

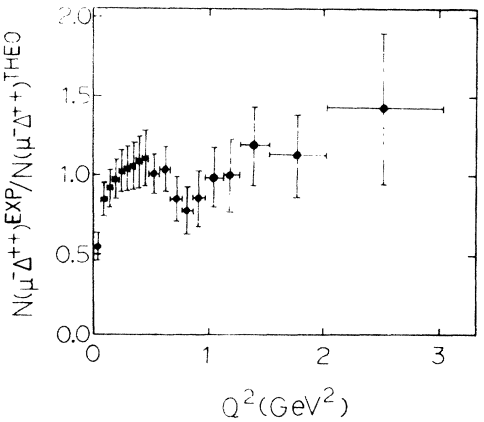

FIG. 11. Ratio of $N^{\text{expt}}(\mu^-\Delta^{++})/N^{\text{theo}}(\mu^-\Delta^{++})$ as a function of Q^2 for the events with $0.3 < E_\nu < 6.0$ GeV.

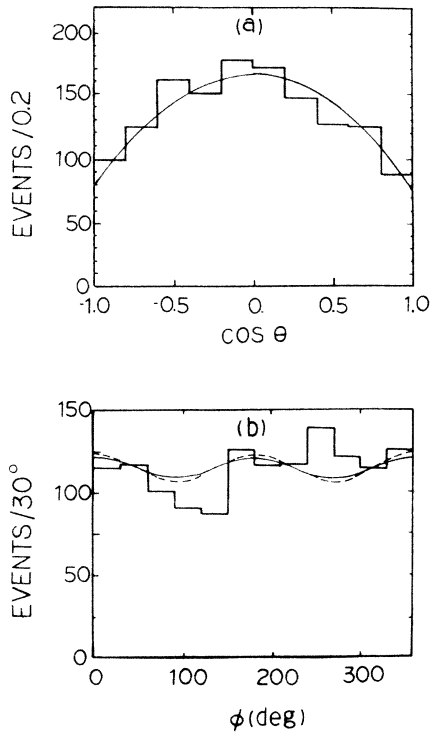

FIG. 12. Decay angular distributions of (a) $\cos\theta$ and (b) azimuthal angle φ for the final state $\mu^- p\pi^+$ with $M(p\pi^+)<1.4$ GeV and $0.5<E_\nu<6.0$ GeV. The solid curves are obtained from the measured density matrix elements. The dashed curves are the predictions of the Adler model with $M_A=1.28$ GeV.

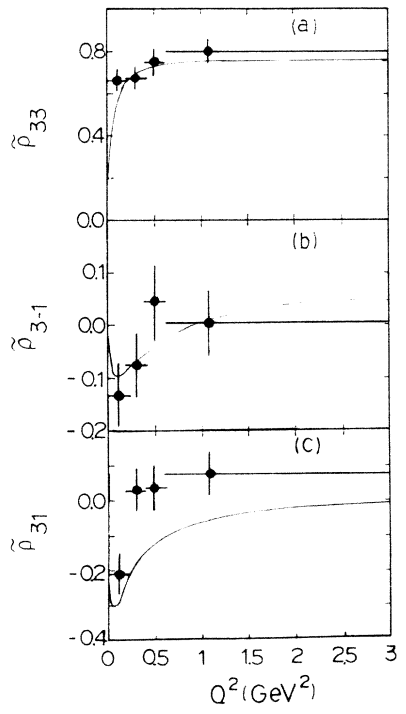

FIG. 13. Density matrix elements as a function of Q^2 for $0.5<E_\nu<6.0$ GeV. The curves are the predictions of the Adler model with $M_A=1.28$ GeV.

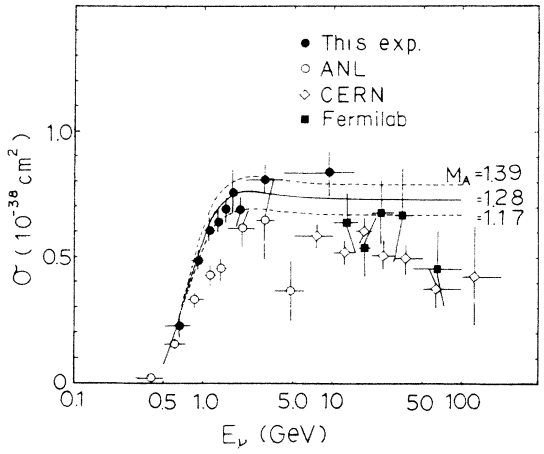

FIG. 14. Comparison of Δ^{++} production cross sections. The solid curve is from the prediction of the Adler model with $M_A=1.28$ GeV. The dashed lines correspond to the predictions with $M_A=1.28\pm0.11$ GeV.

$$\tilde{\rho}_{33}=\tfrac{1}{2}+\tfrac{1}{2}(\rho_{33}+\rho_{-3-3}-\rho_{11}-\rho_{-1-1})\,,$$
$$\tilde{\rho}_{31}=\rho_{31}-\rho_{-1-3}\,, \qquad (11)$$
$$\tilde{\rho}_{3-1}=\rho_{3-1}+\rho_{1-3}\,.$$

The function $dW(\theta,\phi)/d\Omega$ depends on the dynamical structure of the formation and the decay of the Δ^{++} including the spin of the W boson. Using Eq. (10), the reduced density matrix elements $\tilde{\rho}_{mn}$ were determined as a

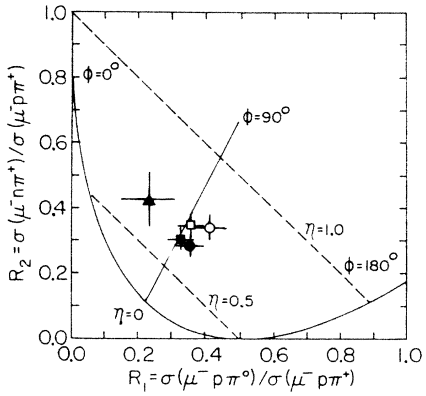

FIG. 15. Plot of the cross-section ratios $R_1=\sigma(\mu^- p\pi^0)/\sigma(\mu^- p\pi^+)$ and $R_2=\sigma(\mu^- n\pi^+)/\sigma(\mu^- p\pi^+)$ for $0.5<E_\nu<3.0$ GeV. The dashed straight lines and the solid lines correspond to constant values of $\eta=|A_{1/2}|/|A_{3/2}|$ and the relative phase angle φ, respectively. The data points are solid circle, $M(N\pi)<1.4$ GeV; open circle, $M(N\pi)<1.6$ GeV from this experiment; solid square, $M(N\pi)<1.4$ GeV; open square, $M(N\pi)<1.6$ GeV from Ref. 5; and triangle, $M(N\pi)<1.4$ GeV from Ref. 13.

TABLE V. Results of the isospin analysis ($0.5 < E_\nu < 3$ GeV).

	$M(N\pi)$ no cut	$M(N\pi) < 1.6$ GeV	$M(N\pi) < 1.4$ GeV
R_1	0.442±0.060	0.416±0.054	0.354±0.044
R_2	0.357±0.044	0.339±0.042	0.284±0.034
η	0.836±0.067	0.795±0.064	0.676±0.062
φ (deg)	100.07 ±6.41	98.60 ±6.03	95.76 ±5.71

function of Q^2 and they are displayed in Figs. 13(a)–13(c). The curves in Fig. 13 are the predictions of the Adler model[11] which describes the data well except for $\tilde{\rho}_{31}$. The solid curves in Fig. 12 were obtained by using the measured values of $\tilde{\rho}_{mn}$ in the region of $Q^2 < 3.0$ GeV^2. The dashed curves in Fig. 12 are the prediction of the Adler model and they are in good agreement with our data. The dashed curve in Fig. 12(a) overlaps with the solid curve.

Figure 14 shows the Δ^{++} production cross section from this experiment. For comparison, the ANL (Ref. 5), Fermilab,[4] and CERN data[6] are also displayed. The curve is the prediction of the Adler model[11] with the axial-vector mass $M_A = 1.28$ GeV, which describes the data well within the errors.

C. Isospin structure of the πN system

An isospin analysis of the πN system in $\nu_\mu + d$ interactions can provide information on the isospin amplitudes of the πN states as well as on the isospin structure of the exchange amplitudes. Since the well-established standard model only has isovector exchange amplitudes, we analyzed the πN system only in terms of the isovector amplitude and did not include an isotensor exchange amplitude.

The amplitudes for the $\mu^- p\pi^+$, $\mu^- p\pi^0$, and $\mu^- n\pi^+$ states can be written in terms of the isospin $I = \frac{1}{2}$ and $I = \frac{3}{2}$ complex amplitudes $A_{1/2}$ and $A_{3/2}$ for the πN system as

$$
\begin{aligned}
A(\mu^- p\pi^+) &= A_{3/2} , \\
A(\mu^- p\pi^0) &= \frac{\sqrt{2}}{3}(A_{3/2} - A_{1/2}) , \\
A(\mu^- n\pi^+) &= \tfrac{1}{3}(A_{3/2} + 2A_{1/2}) .
\end{aligned}
\tag{12}
$$

Defining η and ρ as

$$
\eta = \frac{|A_{1/2}|}{|A_{3/2}|} ,
$$

$\varphi =$ the relative phase angle between $A_{1/2}$ and $A_{3/2}$, the quantities, R_1 and R_2 are given by

$$
\begin{aligned}
R_1 &= \frac{\sigma(\mu^- p\pi^0)}{\sigma(\mu^- p\pi^+)} = \tfrac{2}{9}(1 + \eta^2 - 2\eta\cos\varphi) , \\
R_2 &= \frac{\sigma(\mu^- n\pi^+)}{\sigma(\mu^- p\pi^+)} = \tfrac{1}{9}(1 + 4\eta^2 - 4\eta\cos\varphi) .
\end{aligned}
$$

The quantities R_1, R_2, η, and φ were determined using the corrected numbers of $\mu^- p\pi^+$, $\mu^- p\pi^0$, and $\mu^- n\pi^+$ events with $E_\nu = 0.5 - 3.0$ GeV. This neutrino energy range was chosen to be the same as that in the other experiments[5,7,13] so that the results can be directly compared. The results for various $M(N\pi)$ cuts are summarized in Table V.

Figure 15 shows the scatter plot of R_1 vs R_2 for the two mass cuts, $M(N\pi) < 1.4$ and $M(N\pi) < 1.6$ GeV, together with the results from other experiments.[5,13] These results indicate that the $I = \frac{1}{2}$ amplitude is comparable in size and almost orthogonal to the $I = \frac{3}{2}$ amplitude. Our final results are in good agreement with those of the previous BNL experiment[7] and of the ANL 12-foot experiment,[5] while they are not in such good agreement with the Gargamell results.[13]

Figure 16 shows the ratio $\eta = A_{1/2}/A_{3/2}$ as a function of $M(N\pi)$. The $I = \frac{1}{2}$ amplitude rapidly increases from $M(N\pi) = 1.4$ GeV, indicating the dominant $I = \frac{1}{2}$ component of the high-mass region.

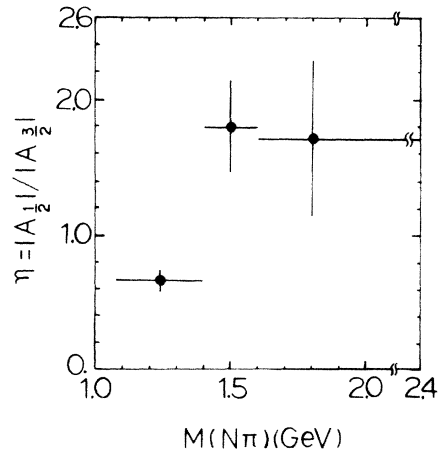

FIG. 16. Ratio of isospin amplitude $|A_{1/2}|/|A_{3/2}|$ as a function of $M(N\pi)$ for $0.5 < E_\nu < 3.0$ GeV.

IV. MULTIPION PRODUCTION

Figures 17(a) and 17(b) show the $p\pi^+$- and the $\pi^+\pi^-$-mass distributions obtained from the 276 $\mu^- p\pi^+\pi^-$ events. The dominant peak seen in the $p\pi^+$-mass distribution is attributed to the $\Delta^{++}(1232)$. No other high-mass Δ production is observed. The shaded area in Fig 17(b) corresponds to the events with $M(p\pi^+) > 1.4$ GeV. No apparent ρ^0 production is observed. The broad peak near the $\pi\pi$ threshold is a reflection from the Δ^{++} events.

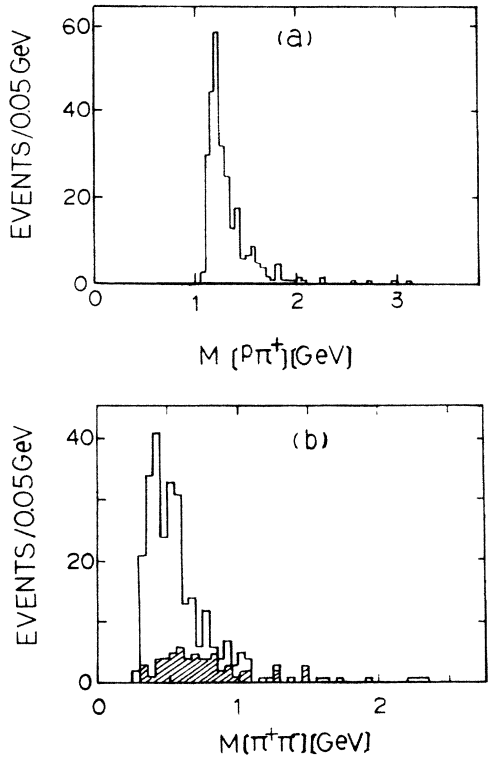

FIG. 17. Mass distributions of (a) $M(p\pi^+)$ and (b) $M(\pi^+\pi^-)$ for the $\mu^-p\pi^+\pi^-$ state. The shaded area represents the events with $M(p\pi^+) > 1.4$ GeV.

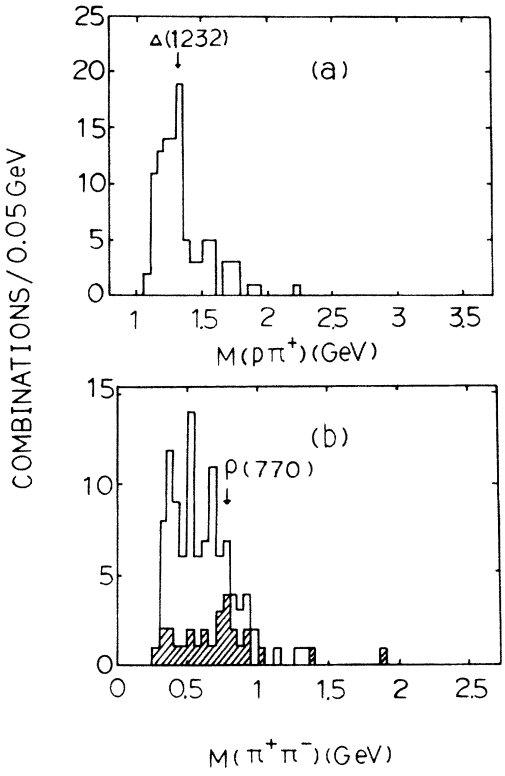

FIG. 18. Mass distributions of (a) $M(p\pi^+)$ and (b) $M(\pi^+\pi^-)$ for the $\mu^-p\pi^+\pi^+\pi^-$ state. The shaded area represents the events with $M(p\pi^+) > 1.4$ GeV.

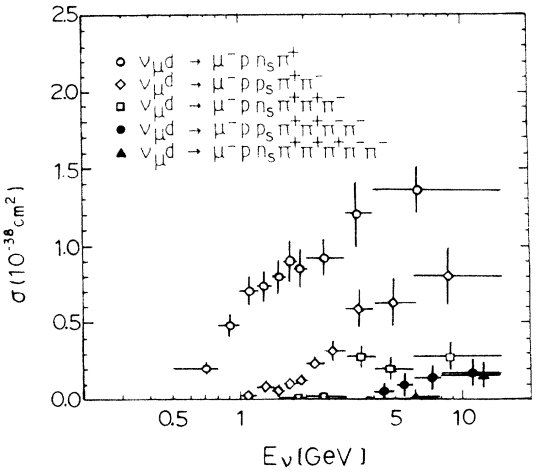

FIG. 19. Single and multipion production cross sections as a function of E_ν.

Figures 18(a) and 18(b) show the $p\pi^+$- and the $\pi^+\pi^-$-mass distributions for the 53 $\mu^-p\pi^+\pi^+\pi^-$ events. In the $p\pi^+$-mass distribution, the $\Delta^{++}(1232)$ is apparent. In the $\pi^+\pi^-$-mass distribution, no significant ρ^0 signal is observed. However, there is a hint of ρ^0 production in the shaded distribution, where the $\pi^+\pi^-$ mass is plotted using the same π^+ in the $p\pi^+$ combination if the $p\pi^+$ mass is greater than 1.4 GeV.

Figure 19 shows the new results for the cross sections of exclusive multipion production in $\nu_\mu d$ interactions for $E_\nu < 15$ GeV. For comparison, the cross section for the reaction $\nu d \rightarrow \mu^- p\pi^+ n_s$ measured in this experiment is

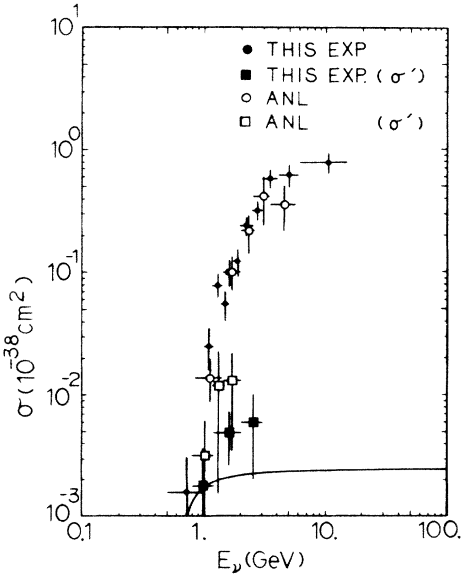

FIG. 20. Comparison of the two-pion production cross sections. The solid and open circles are the total two-pion production cross sections from this experiment and Ref. 2. The solid and open squares are the threshold cross sections from this experiment and Ref. 2.

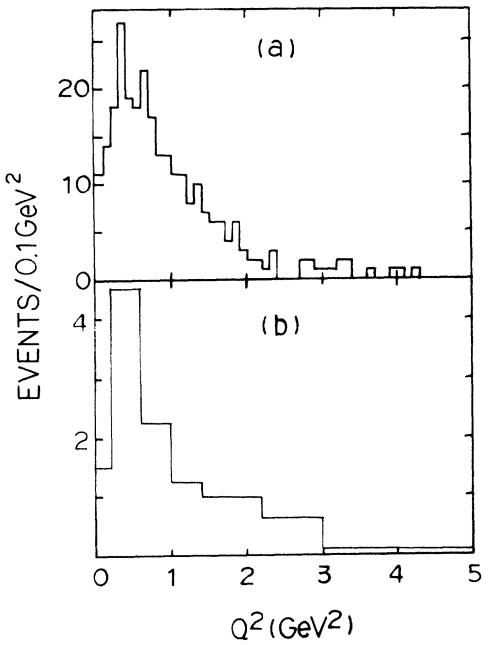

FIG. 21. Distributions of dN/dQ^2 for (a) $\mu^-p\pi^+\pi^-$ and (b) $\mu^-p\pi^+\pi^+\pi^-$ events.

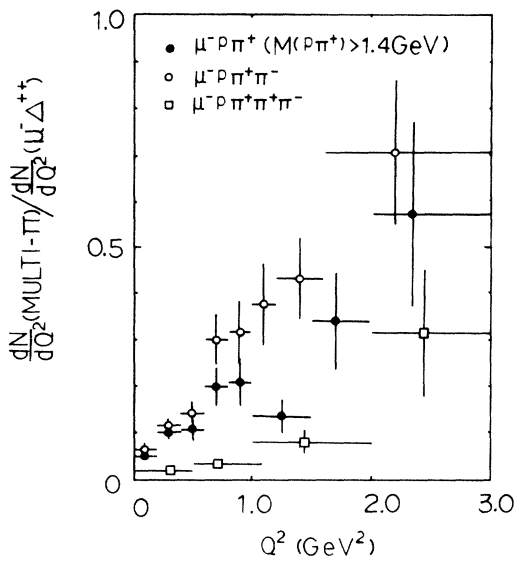

FIG. 22. Ratios of dN/dQ^2 of reactions (5) and (6) to that of $dN/dQ^2(\mu^-\Delta^{++})$. The ratios for the $\mu^-p\pi^+$ with $M(p\pi^+)>1.4$ GeV are also shown.

also displayed. The cross sections rise from the threshold and plateau in the range of E_ν between 3 and 15 GeV.

Figure 20 shows the cross section for dipion production in $\nu d\to\mu^-p\pi^+\pi^-p_s$ from this experiment and the ANL experiment.[2] They are in good agreement.

The theoretical predictions of weak dipion production in the reaction $\nu n\to\mu^-p\pi^+\pi^-$ close to threshold have been calculated by Adjei *et al.*[14] to determine the chiral-symmetry-breaking parameter obtained from the study of two-pion production in $\pi N\to N\pi\pi$. To compare with this model, we extracted $\mu^-p\pi^+\pi^-$ events in the threshold region defined by Adjei *et al.* as

$$|M(\pi^+\pi^-)-2m_\pi|<\tfrac{3}{4}m_\pi\ ,$$

$$|M(p_i\pi^+\pi^-)-M_p-2m_\pi|<\tfrac{3}{4}m_\pi\ ,$$

$$|M(p_f\pi^+\pi^-)-M_p-2m_\pi|<\tfrac{3}{4}m_\pi\ ,$$

where p_i and p_f are the initial and final proton and m_π and M_p are the pion and proton masses, respectively.

Figure 20 shows the cross section σ' for the selected events in the threshold region together with the ANL results.[2] The curve is the model prediction of the cross section σ' and it is lower than the data points.

Figures 21(a) and 21(b) show the Q^2 distributions for the $\mu^-p\pi^+\pi^-$ and $\mu^-p\pi^+\pi^+\pi^-$ events. To compare with the Q^2 distribution of the quasi-two-body reaction $\nu p\to\mu^-\Delta^{++}$. The ratios of dN/dQ^2 for reactions (5) and (6) to that for the reaction $\nu p\to\mu^-\Delta^{++}$ as a function of Q^2 are shown in Fig. 22. The ratios for the $\mu^-p\pi^+$ events with $M(p\pi^+)>1.4$ GeV are also shown. This mass cut was imposed to remove the quasi-two-body reaction $\nu p\to\mu^-\Delta^{++}$. The ratios all increase as Q^2 increases, indicating an apparent difference in the production mechanism for these inelastic reactions compared to the two-body neutrino reactions.

ACKNOWLEDGMENTS

We would like to thank the AGS staff, the crews of the 7-foot bubble chamber, and the scanning and measuring personnel both at BNL and at Tohoku University for their dedicated efforts. This research was supported by the U.S.-Japan Cooperative Research Project on High Energy Physics under the Ministry of Education, Science, and Culture of Japan and the U.S. Department of Energy under Contract No. DE-AC02-76-CH00016.

*Present address: University of Maryland, College Park, Maryland 20742.
†Permanent address: Toshiba Electric Company, Kawasaki, Japan.
‡Permanent address: KEK, Ibaraki, Japan.
§Permanent address: Fujitsu Company, Tokyo, Japan.
**Present address: CERN, CH-1211 Geneva 23, Switzerland.
††Deceased.

[1]S. J. Barish *et al.*, Phys. Rev. D **19**, 2521 (1979); J. Bell *et al.*, Phys. Rev. Lett. **41**, 1012 (1978).
[2]D. Day *et al.*, Phys. Rev. D **28**, 2714 (1983).
[3]J. Bell *et al.*, Phys. Rev. Lett. **40**, 1226 (1978).
[4]J. Bell *et al.*, Phys. Rev. Lett. **41**, 1008 (1978).
[5]G. M. Radecky *et al.*, Phys. Rev. D **25**, 1161 (1982).
[6]P. Allen *et al.*, Nucl. Phys. **B176**, 269 (1980).
[7]N. J. Baker *et al.*, Phys. Rev. D **23**, 2495 (1981).

[8]N. J. Baker *et al.*, Phys. Rev. D **23**, 2499 (1981).
[9]N. J. Baker *et al.*, Phys. Rev. D **28**, 2900 (1983); **25**, 617 (1982); **24**, 2779 (1981).
[10]T. Kitagaki *et al.*, Tohoku University Report No. TUHEP 85-03, 1985 (unpublished).
[11]P. A. Schreiner and F. Von Hippel, Nucl. Phys. B **58**, 333 (1973).
[12]S. L. Adler, Ann. Phys. (N.Y.) **50**, 189 (1968); Phys. Rev. D **12**, 2644 (1975).
[13]M. Pohl *et al.*, Lett. Nuovo Cimento **24**, 540 (1979).
[14]S. A. Adjei *et al.*, Phys. Rev. D **24**, 623 (1981).